Chapter 6
Combined Helmholtz Equation Least-Squares (CHELS) Method

Although the HELS method has exhibited a great promise in reconstructing the acoustic fields in both exterior and interior regions, the accuracy in reconstruction for an arbitrarily shaped structure can be unsatisfactory. This is because the expansion based on the spherical waves for an acoustic field generated by on an arbitrarily shaped surface is incomplete.

An alternative for reconstructing acoustic radiation from an arbitrary structure is to use the Helmholtz integral theory. In implementing this integral theory, BEM is used and the surface is discretized into segments and the acoustic field is specified on the nodes of these segments using a particular interpolation scheme. This BEM-based NAH has been used to reconstructing acoustic radiation from structures in the exterior and interior regions.

The main advantage of the BEM-based NAH is its generality, allowing users to tackle an arbitrarily shaped structure. The disadvantage is that it may fail to yield a unique solution for the exterior problem when the excitation frequencies are close to one of the eigenfrequencies of the boundary value problem in the corresponding interior region. While this nonuniqueness difficulty may be overcome by the CHIEF method, the efficiency and accuracy of its reconstruction can be significantly affected.

The main drawback of the BEM-based NAH, however, is due to the fact that the acoustic field is reconstructed via spatial discretization. In other words, we must have a minimum number of nodes per wavelength in order to achieve the desired resolution in reconstruction. Accordingly, one must take enough measurements of the radiated acoustic pressures to determine the acoustic quantities specified on discrete nodes. For complex structures vibrating at mid-to-high frequencies, the number of nodes necessary to describe the surface acoustic quantities can be large. Hence the number of measurements is large, which makes the reconstruction process very time consuming. Although there are techniques developed recently to avoid the singularity problem inherent in the Helmholtz integral equation and methodologies to optimize the measurement locations by using an effective

S.F. Wu, *The Helmholtz Equation Least Squares Method*, Modern Acoustics and Signal Processing, DOI 10.1007/978-1-4939-1640-5_6

independence [27] implementation of the BEM-based NAH is not straightforward and reconstruction of the acoustic field is extremely slow and inefficient.

It is emphasized that in using the BEM-based NAH it is not necessary to have exactly the same measurements as discrete nodes. This is because using SVD and regularization procedures, one can have either an over- or under-determined systems of equations. Accordingly, one can use fewer measurements than the discrete nodes. However, the accuracy of reconstruction cannot be guaranteed if the measurements are substantially fewer than the discrete nodes. This is because the measured data are not error free and background noises are always present. In order to obtain a convergent solution, the equation must be truncated to filter out the evanescent waves that fall under the background noises. If measurements are too few, the equivalent cutoff wavenumber is forced to be very low. As a result, the high spatial wavenumber contents are filtered out and aliasing occurs in reconstruction.

In this chapter we show that by combining the HELS- and BEM-based NAH, the efficiency of reconstruction can be significantly enhanced and satisfactory reconstruction be obtained by using relatively few measurements [91]. First, we present a brief account of the Helmholtz integral theory.

6.1 The Helmholtz Integral Theory

The key to the acoustic radiation problems is to solve the wave equation subject to certain boundary conditions, which for a harmonic excitation reduces to the Helmholtz equation

$$\nabla^2 \hat{p}\left(\vec{x};\omega\right) + k^2 \hat{p}\left(\vec{x};\omega\right) = 0, \tag{6.1}$$

where $\hat{p}\left(\vec{x};\omega\right)$ is the complex amplitude of the acoustic pressure at any field point $\vec{x}$ and satisfies the Sommerfeld radiation condition at infinity,

$$\lim_{\left|\vec{x}\right|\to\infty} \left|\vec{x}\right| \left(\frac{\partial \hat{p}}{\partial \left|\vec{x}\right|} - ik\hat{p} \right) = 0 \quad \text{as} \quad \left|\vec{x}\right| \to \infty. \tag{6.2}$$

The Helmholtz equation (6.1) subject to the boundary condition can be solved for source surfaces that are expressible as one of 11 coordinate systems [92]. For arbitrary geometry, there is no analytic solution; hence, numerical solutions are sought. However, the efforts involved may be significant because one must discretize the entire three-dimensional space.

To enhance the efficiency in numerical computations, we can utilize the Helmholtz integral theory, which can be derived by making use of the free-space Green's function. First, we consider the inhomogeneous Helmholtz equation for the free-space Green's function,

$$\nabla^2 G\left(\vec{x}\middle|\vec{x}_s;\omega\right) + k^2 G\left(\vec{x}\middle|\vec{x}_s;\omega\right) = -4\pi\delta\left(\vec{x} - \vec{x}_s\right), \tag{6.3}$$

where $G = \mathrm{e}^{ikR}/R$, where $R = \left|\vec{x} - \vec{x}_s\right|$ is the distance between the source at $\vec{x}_s$ and a receiver at $\vec{x}$ in free space, and $\delta\left(\vec{x} - \vec{x}_s\right)$ is the Dirac delta function [93], which can be considered as a function that is 0 everywhere except at the origin, where it is infinite,

$$\delta(x - x_0) = \begin{cases} 0, & x \neq x_0 \\ \infty, & x = x_0 \end{cases}. \tag{6.4}$$

The Dirac delta function has the sifting property,

$$\int_{-\infty}^{\infty} \delta(x - x_0) f(x) dx = f(x_0). \tag{6.5}$$

Therefore, for $f(x) \equiv 1$, the integration of the Dirac delta function is identically unity,

$$\int_{-\infty}^{\infty} \delta(x - x_0) dx = 1 \tag{6.6}$$

Multiply Eq. (6.1) by G and Eq. (6.3) by $\hat{p}\left(\vec{x};\omega\right)$, and use the chain rule to rewrite the Laplacian operator ∇^2 as

$$\begin{aligned} &\nabla \cdot \left[G\left(\vec{x}\middle|\vec{x}_s;\omega\right)\nabla\hat{p}\left(\vec{x};\omega\right)\right] - \nabla G\left(\vec{x}\middle|\vec{x}_s;\omega\right)\cdot\nabla\hat{p}\left(\vec{x};\omega\right) \\ &\quad + k^2 G\left(\vec{x}\middle|\vec{x}_s;\omega\right)\hat{p}\left(\vec{x};\omega\right) = 0, \end{aligned} \tag{6.7}$$

$$\begin{aligned} &\nabla \cdot \left[\hat{p}\left(\vec{x};\omega\right)\nabla G\left(\vec{x}\middle|\vec{x}_s;\omega\right)\right] - \nabla G\left(\vec{x}\middle|\vec{x}_s;\omega\right)\cdot\nabla\hat{p}\left(\vec{x};\omega\right) \\ &\quad + k^2 G\left(\vec{x}\middle|\vec{x}_s;\omega\right)\hat{p}\left(\vec{x};\omega\right) = -4\pi\hat{p}\left(\vec{x};\omega\right)\delta\left(\vec{x} - \vec{x}_s\right). \end{aligned} \tag{6.8}$$

Subtracting Eq. (6.8) from (6.7) and integrating both sides over the volume enclosed by the source surface and that at infinity leads to

$$\iiint\limits_V \nabla\cdot\left[G\left(\vec{x}\middle|\vec{x}_s;\omega\right)\nabla\hat{p}\left(\vec{x};\omega\right)-\hat{p}\left(\vec{x};\omega\right)\nabla G\left(\vec{x}\middle|\vec{x}_s;\omega\right)\right]dV$$
$$=4\pi\iiint\limits_V \hat{p}\left(\vec{x};\omega\right)\delta\left(\vec{x}-\vec{x}_s\right)dV. \tag{6.9}$$

The volume integral on the right side of Eq. (6.9) leads to the acoustic pressure itself due to the sifting property of the Dirac delta function Eq. (6.5). The volume integral on the left side can be expressed as a surface integral by using the Gauss theorem or divergence theorem [94],

$$\hat{p}\left(\vec{x};\omega\right)=\frac{1}{4\pi}\iint\limits_{S'}\left[\hat{p}\left(\vec{x}_{s'};\omega\right)\frac{\partial G\left(\vec{x}\middle|\vec{x}_{s'};\omega\right)}{\partial \mathrm{n}\left(\vec{x}_{s'}\right)}-\frac{\partial\hat{p}\left(\vec{x}_{s'};\omega\right)}{\partial \mathrm{n}\left(\vec{x}_{s'}\right)}G\left(\vec{x}\middle|\vec{x}_{s'};\omega\right)\right]dS', \tag{6.10}$$

where $\partial/\partial\mathrm{n}$ represents a normal derivative with respect to the outward unit vector on the surface S, and $\partial\hat{p}/\partial\mathrm{n}$ is related to the normal surface velocity through the Euler's equation,

$$\frac{\partial\hat{p}\left(\vec{x}_s;\omega\right)}{\partial\mathrm{n}\left(\vec{x}_s\right)}=i\omega\rho_0\hat{v}_{\mathrm{n}}\left(\vec{x}_s;\omega\right). \tag{6.11}$$

Note that there is a change in sign on the right side of Eq. (6.10) because the unit normal vector on the source surface S, which points to the interior region enclosed by S as required by the Gauss theorem, should point into the region external to S in the surface integral.

Equation (6.10) is known as the Helmholtz integral formulation, which states that $\hat{p}\left(\vec{x};\omega\right)$ anywhere in free space may be specified by integrating the surface acoustic $\hat{p}\left(\vec{x}_s;\omega\right)$ and normal surface velocity $\hat{v}_{\mathrm{n}}\left(\vec{x}_s;\omega\right)$ through the free-space Green's function $G\left(\vec{x}\middle|\vec{x}_s;\omega\right)$. Accordingly, the dimensionality of the original problem given by Eq. (6.1) is reduced by 1.

Note that the surface acoustic pressure $\hat{p}\left(\vec{x}_s;\omega\right)$ and normal surface velocity $\hat{v}_{\mathrm{n}}\left(\vec{x}_s;\omega\right)$ are interrelated together and should not be specified simultaneously in practice. For acoustic radiation problems, the normal surface velocity $\hat{v}_{\mathrm{n}}\left(\vec{x}_s;\omega\right)$ is usually specified in the boundary condition. So the first step in predicting the radiated acoustic pressure $\hat{p}\left(\vec{x};\omega\right)$ is to specify the surface acoustic pressure

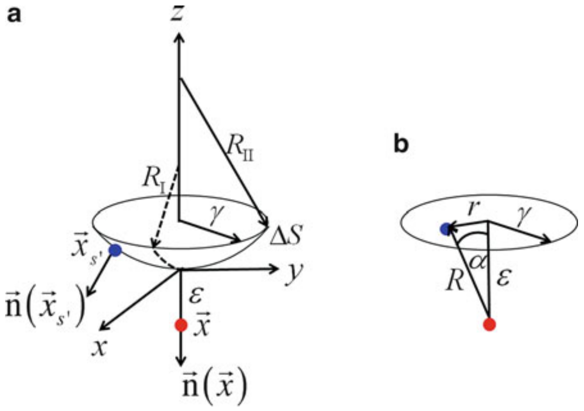

Fig. 6.1 Schematic of taking the limit as the field point approaches the surface $\vec{x} \to \vec{x}_s$. (**a**) The field point is located at $\vec{x} = \vec{x}_s + \varepsilon \vec{n}\left(\vec{x}_s\right)$, the surface point is at $\vec{x}_{s'}$ with the unit normal $\vec{n}\left(\vec{x}_{s'}\right)$, and the distance between these two points is $R = \left|\vec{x} - \vec{x}_{s'}\right|$. (**b**) Close-up view of taking the limit as $R \to 0$. The correct sequence is to take $\varepsilon \to 0$ first, and then $\gamma \to 0$

$\hat{p}\left(\vec{x}_s; \omega\right)$. This may be done by solving an integral equation obtained by taking the limit as the field point approaches the surface $\vec{x} \to \vec{x}_s$ in Eq. (6.10). Note that all integrands in Eq. (6.10) become singular because $R \to 0$ as $\vec{x} \to \vec{x}_s$. This difficulty can be overcome by taking the Cauchy principal value [95]. It is emphasized that the sequence in which this limit is taken is critical. A wrong sequence in taking the limit $\vec{x} \to \vec{x}_s$ leads to a wrong result.

Figure 6.1 depicts schematic of taking the limit $\vec{x} \to \vec{x}_s$. For simplicity yet without loss of generality, we consider the case in which both $\vec{x}_{s'}$ and $\vec{x}_s$ are located inside ΔS, which is a circular segment of the source surface S, centered at $\vec{x}_s$ of a radius γ. The segment ΔS is shaped like a bowl with radii R_{I} and R_{II} in the perpendicular directions, respectively. The remainder of the surface is denoted as $(S - \Delta S)$. The field point is at $\vec{x} = \vec{x}_s + \varepsilon \vec{n}\left(\vec{x}_s\right)$, which is a small distance ε away from the surface point $\vec{x}_s$ along the unit normal direction $\vec{n}\left(\vec{x}_s\right)$. Therefore the distance between these two points is $R = \left|\vec{x} - \vec{x}_{s'}\right|$ (see Fig. 6.1a). As $\vec{x} \to \vec{x}_s$, $R \to 0$ and all integrands in Eq. (6.10) become singular. So care must be taken in taking the limit of $\vec{x} \to \vec{x}_s$.

Note that if $\vec{x}_{s'}$ is in $(S - \Delta S)$, R will not be 0 as $\vec{x} \to \vec{x}_s$, and all integrands in Eq. (6.10) will be finite. So we only need to concentrate on the situation in which $\vec{x}_{s'}$ falls inside ΔS.

Given that ΔS is small, the z component of a generic surface point $\vec{x}_{s'}$ can be expanded into a power series of x, y, R_{I}, and R_{II}, where $x/R_{\mathrm{I}} \ll 1$ and $y/R_{\mathrm{II}} \ll 1$,

$$z = C\sqrt{1-\left(\frac{x^2}{R_{\mathrm{I}}^2}+\frac{y^2}{R_{\mathrm{II}}^2}\right)} \approx C\left(1-\frac{x^2}{2R_{\mathrm{I}}^2}-\frac{y^2}{2R_{\mathrm{II}}^2}\right). \tag{6.12}$$

Equation (6.12) is derived from the ellipsoid equation $(x^2/R_{\mathrm{I}}^2)+(y^2/R_{\mathrm{II}}^2)+(z^2/C^2)=1$, where C is a constant. Therefore for $x/R_{\mathrm{I}} \ll 1$ and $y/R_{\mathrm{II}} \ll 1$, we have

$$z - C \approx -\frac{Cx^2}{2R_{\mathrm{I}}^2}-\frac{Cy^2}{2R_{\mathrm{II}}^2}. \tag{6.13}$$

By using $(z-C)$, we have moved the origin of the coordinate system describing the ellipsoid to the surface point $\vec{x}_s$. The unit outward normal vector $\vec{\mathrm{n}}\left(\vec{x}_{s'}\right)$ at $\vec{x}_{s'}$ can now be approximated by

$$\vec{\mathrm{n}}\left(\vec{x}_{s'}\right) \approx \left(\frac{x}{R_{\mathrm{I}}}\right)\vec{e}_x + \left(\frac{y}{R_{\mathrm{II}}}\right)\vec{e}_y + \vec{e}_z, \tag{6.14}$$

because $\vec{x}_{s'} = x\vec{e}_x + y\vec{e}_y + (z-C)\vec{e}_z$. Similarly, $\vec{x} = \vec{x}_s + \varepsilon\vec{\mathrm{n}}\left(\vec{x}_s\right) = \varepsilon\vec{e}_z$. Thus $\vec{R} = \vec{x} - \vec{x}_{s'}$ is given by

$$\begin{aligned}\vec{R} &= \varepsilon\vec{e}_z - x\vec{e}_x - y\vec{e}_y - (z-C)\vec{e}_z \\ &\approx \left(\varepsilon - \frac{Cx^2}{2R_{\mathrm{I}}^2}-\frac{Cy^2}{2R_{\mathrm{II}}^2}\right)\vec{e}_z - x\vec{e}_x - y\vec{e}_y,\end{aligned} \tag{6.15}$$

and the normal derivative of the free-space Green's function $\partial G\left(\vec{x}\middle|\vec{x}_s;\omega\right)/\partial\mathrm{n}$ in Eq. (6.10) is

$$\begin{aligned}\frac{\partial G\left(\vec{x}\middle|\vec{x}_{s'};\omega\right)}{\partial\mathrm{n}\left(\vec{x}_{s'}\right)} &= \vec{\mathrm{n}}\left(\vec{x}_{s'}\right)\cdot\nabla_{s'}G\left(\vec{x}\middle|\vec{x}_{s'};\omega\right) \\ &\approx -\left(\frac{x}{R_{\mathrm{I}}}\vec{e}_x + \frac{y}{R_{\mathrm{II}}}\vec{e}_y + \vec{e}_z\right)\cdot\left(\frac{ikR-1}{R^2}\right)\left(\frac{\vec{x}-\vec{x}_{s'}}{R}\right)\mathrm{e}^{ikR} \\ &= \left(\frac{x}{R_{\mathrm{I}}}\vec{e}_x + \frac{y}{R_{\mathrm{II}}}\vec{e}_y + \vec{e}_z\right)\cdot\left[\frac{x\vec{e}_x + y\vec{e}_y - \left(\varepsilon + \frac{Cx^2}{2R_{\mathrm{I}}^2}+\frac{Cy^2}{2R_{\mathrm{II}}^2}\right)\vec{e}_z}{R^3}\right](ikR-1)\mathrm{e}^{ikR}, \\ &\approx \left(\frac{x^2}{R_{\mathrm{I}}}+\frac{y^2}{R_{\mathrm{II}}}-\varepsilon-\frac{Cx^2}{2R_{\mathrm{I}}^2}-\frac{Cy^2}{2R_{\mathrm{II}}^2}\right)(ikR-1)(1+ikR) = \left(\varepsilon-\frac{Cx^2}{2R_{\mathrm{I}}^2}-\frac{Cy^2}{2R_{\mathrm{II}}^2}\right)\frac{\left(1+k^2R^2\right)}{R^3}\end{aligned} \tag{6.16}$$

where we have expanded e^{ikR} into the Taylor series for a small R as $R \to 0$, and R is written as

$$R = \sqrt{x^2 + y^2 + (\varepsilon - z)^2} \approx \sqrt{\varepsilon^2 + x^2 + y^2} = \sqrt{\varepsilon^2 + r^2}. \tag{6.17}$$

Meanwhile, Fig. 6.1b implies that for a small area ΔS, $dS \approx rdr$, $x = r\cos\phi$, and $y = r\sin\phi$, where r varies from 0 to γ and ϕ from 0 to 2π. With Eqs. (6.16) and (6.17) we can evaluate the integrals in Eq. (6.10) as $\vec{x} \to \vec{x}_s$. Let us consider the first integral on the right side of Eq. (6.10). In particular, we divide the surface into ΔS and $(S - \Delta S)$ in taking the limit as $\Delta S \to 0$,

$$\begin{aligned}\iint\limits_{S} \hat{p}\left(\vec{x}_{s'};\omega\right)\frac{\partial G\left(\vec{x}_s\middle|\vec{x}_{s'};\omega\right)}{\partial \mathrm{n}\left(\vec{x}_{s'}\right)}dS' &= \lim_{\Delta S\to 0}\iint\limits_{\Delta S}\hat{p}\left(\vec{x}_{s'};\omega\right)\frac{\partial G\left(\vec{x}_s\middle|\vec{x}_{s'};\omega\right)}{\partial \mathrm{n}\left(\vec{x}_{s'}\right)}dS' \\ &+ \lim_{\Delta S\to 0}\iint\limits_{S-\Delta S}\hat{p}\left(\vec{x}_{s'};\omega\right)\frac{\partial G\left(\vec{x}_s\middle|\vec{x}_{s'};\omega\right)}{\partial \mathrm{n}\left(\vec{x}_{s'}\right)}dS',\end{aligned} \tag{6.18}$$

where all surface points in the first integral fall inside ΔS so that as $\vec{x} \to \vec{x}_{\mathrm{s}}, R \to 0$. For the second integral, $\vec{x}_s$ is in $(S - \Delta S)$, while $\vec{x}_{s'}$ is in ΔS. Hence as $\vec{x} \to \vec{x}_s$, $R \neq 0$. So we only need to focus on the first integral on the right side of Eq. (6.18) because the second integral is regular as the field point approaches the surface $\vec{x} \to \vec{x}_s$.

The required limit $\Delta S \to 0$ in Eq. (6.18) can be accomplished by taking $\varepsilon \to 0$ with γ fixed, followed by $\gamma \to 0$. The order in which these limits are taken is very important.

Substituting Eqs. (6.16) and (6.17) into the first integral on the right side of Eq. (6.18) yields

$$\begin{aligned}\lim_{\Delta S\to 0}\iint\limits_{\Delta S}\hat{p}\left(\vec{x}_{s'};\omega\right)\frac{\partial G\left(\vec{x}_s\middle|\vec{x}_{s'};\omega\right)}{\partial \mathrm{n}\left(\vec{x}_{s'}\right)}dS' &= \lim_{\substack{\varepsilon\to 0\\ \gamma\to 0}}\iint\limits_{S-\Delta S}\hat{p}\left(\vec{x}_{s'};\omega\right)\frac{\varepsilon}{R^3}rdrd\phi \\ &+ \lim_{\substack{\varepsilon\to 0\\ \gamma\to 0}}\iint\limits_{S-\Delta S}\hat{p}\left(\vec{x}_{s'};\omega\right)\left[\frac{\varepsilon k^2 r}{R} - \frac{k^2 r^3}{2R}\left(\frac{\cos^2\phi}{R_{\mathrm{I}}} + \frac{\sin^2\phi}{R_{\mathrm{II}}}\right)\right]drd\phi \\ &- \lim_{\substack{\varepsilon\to 0\\ \gamma\to 0}}\iint\limits_{S-\Delta S}\frac{\hat{p}\left(\vec{x}_{s'};\omega\right)r^3}{2R^3}\left(\frac{\cos^2\phi}{R_{\mathrm{I}}} + \frac{\sin^2\phi}{R_{\mathrm{II}}}\right)drd\phi.\end{aligned} \tag{6.19}$$

From Fig. 6.1b we see that we can use trigonometric properties to rewrite $r = \varepsilon \tan\alpha$ and $R = \varepsilon \sec\alpha$. Accordingly, we have $dr = \varepsilon \sec^2\alpha d\alpha$, $rdr = \varepsilon^2 \tan\alpha \sec^2\alpha d\alpha$, and $(\varepsilon/R^3) rdr = \sin\alpha d\alpha$. As $\varepsilon \to 0$, $\alpha \to \pi/2$. Therefore, the first integral on the right side of Eq. (6.19) leads to

$$\begin{aligned}\lim_{\substack{\varepsilon\to 0\\ \gamma\to 0}} \iint_{S-\Delta S} \hat{p}\left(\vec{x}_{s'};\omega\right) \frac{\varepsilon}{R^3} r dr d\phi &= \lim_{\substack{\varepsilon\to 0\\ \gamma\to 0}} \int_0^{2\pi}\int_0^{\pi/2} \hat{p}\left(\vec{x}_{s'};\omega\right) \frac{\varepsilon^3 \tan\alpha \sec^2\alpha}{\varepsilon^3 \sec^3\alpha} d\alpha d\phi \\ &= \lim_{\substack{\varepsilon\to 0\\ \gamma\to 0}} \int_0^{2\pi}\int_0^{\pi/2} \hat{p}\left(\vec{x}_{s'};\omega\right) \sin\alpha d\alpha d\phi \\ &= -2\pi\hat{p}\left(\vec{x}_s;\omega\right) \cos\alpha\Big|_0^{2\pi} = 2\pi\hat{p}\left(\vec{x}_s;\omega\right). \end{aligned} \tag{6.20}$$

Note that if we let $\gamma \to 0$ first in Eq. (6.19), the integration limits for α would be all 0, making the integral to vanish, which will be obviously wrong.

The second and third integrals on the right side of Eq. (6.19) are given by

$$\begin{aligned}&\lim_{\substack{\varepsilon\to 0\\ \gamma\to 0}} \iint_{S-\Delta S} \hat{p}\left(\vec{x}_{s'};\omega\right) \left[\frac{\varepsilon k^2 r}{R} - \frac{k^2 r^3}{2R}\left(\frac{\cos^2\phi}{R_{\mathrm{I}}} + \frac{\sin^2\phi}{R_{\mathrm{II}}}\right)\right] dr d\phi \\ &= \lim_{\substack{\varepsilon\to 0\\ \gamma\to 0}} \int_0^{2\pi}\int_0^{\pi/2} \hat{p}\left(\vec{x}_{s'};\omega\right) \left[\frac{k^2\varepsilon^2}{\sec\alpha} - \frac{k^2\varepsilon^3 \tan^2\alpha}{2\sec\alpha}\left(\frac{\cos^2\phi}{R_{\mathrm{I}}} + \frac{\sin^2\phi}{R_{\mathrm{II}}}\right)\right] \tan\alpha \sec^2\alpha d\alpha d\phi \equiv 0. \end{aligned} \tag{6.21}$$

$$\begin{aligned}&\lim_{\substack{\varepsilon\to 0\\ \gamma\to 0}} \iint_{S-\Delta S} \frac{\hat{p}\left(\vec{x}_{s'};\omega\right) r^3}{2R^3} \left(\frac{\cos^2\phi}{R_{\mathrm{I}}} + \frac{\sin^2\phi}{R_{\mathrm{II}}}\right) dr d\phi \\ &= \lim_{\substack{\varepsilon\to 0\\ \gamma\to 0}} \int_0^{2\pi}\int_0^{\pi/2} \frac{\hat{p}\left(\vec{x}_{s'};\omega\right) \varepsilon^2 \tan^3\alpha \sec^2\alpha}{2\varepsilon \sec^3\alpha} \left(\frac{\cos^2\phi}{R_{\mathrm{I}}} + \frac{\sin^2\phi}{R_{\mathrm{II}}}\right) d\alpha d\phi \equiv 0. \end{aligned} \tag{6.22}$$

Meanwhile, the second integral on the right side of Eq. (6.18) is regular as $\Delta S \to 0$. So we have

$$\begin{aligned}&\lim_{\Delta S\to 0} \iint_{S-\Delta S} \hat{p}\left(\vec{x}_{s'};\omega\right) \frac{\partial G\left(\vec{x}_s | \vec{x}_{s'};\omega\right)}{\partial \mathrm{n}\left(\vec{x}_{s'}\right)} dS' \\ &= \iint_{S'} \hat{p}\left(\vec{x}_{s'};\omega\right) \frac{\partial G\left(\vec{x}_s | \vec{x}_{s'};\omega\right)}{\partial \mathrm{n}\left(\vec{x}_{s'}\right)} dS'. \end{aligned} \tag{6.23}$$

Following the same procedures as outlined above, we can show that the second integral on the right side of Eq. (6.10) is regular as the field point approaches the surface,

$$\begin{aligned}\iint_{S'} \frac{\partial \hat{p}\left(\vec{x}_{s'};\omega\right)}{\partial \mathrm{n}\left(\vec{x}_{s'}\right)} G\left(\vec{x}\middle|\vec{x}_{s'};\omega\right) dS' &= \lim_{\Delta S\to 0}\iint_{\Delta S} \frac{\partial \hat{p}\left(\vec{x}_{s'};\omega\right)}{\partial \mathrm{n}\left(\vec{x}_{s'}\right)} G\left(\vec{x}\middle|\vec{x}_{s'};\omega\right) dS' \\ &+ \lim_{\Delta S\to 0}\iint_{S-\Delta S} \frac{\partial \hat{p}\left(\vec{x}_{s'};\omega\right)}{\partial \mathrm{n}\left(\vec{x}_{s'}\right)} G\left(\vec{x}\middle|\vec{x}_{s'};\omega\right) dS' = \iint_{S'} \frac{\partial \hat{p}\left(\vec{x}_{s'};\omega\right)}{\partial \mathrm{n}\left(\vec{x}_{s'}\right)} G\left(\vec{x}\middle|\vec{x}_{s'};\omega\right) dS'.\end{aligned} \tag{6.24}$$

Substituting Eqs. (6.23) and (6.24) into (6.10) with $\vec{x} \to \vec{x}_{\mathrm{s}}$ then leads to

$$\hat{p}\left(\vec{x}_s;\omega\right) = \frac{1}{2\pi}\iint_{S'}\left[\hat{p}\left(\vec{x}_{s'};\omega\right)\frac{\partial G\left(\vec{x}_s\middle|\vec{x}_{s'};\omega\right)}{\partial \mathrm{n}\left(\vec{x}_{s'}\right)} - i\omega\rho_0\hat{v}_{\mathrm{n}}\left(\vec{x}_{s'};\omega\right)G\left(\vec{x}_s\middle|\vec{x}_{s'};\omega\right)\right]dS', \tag{6.25}$$

where both $\vec{x}_s$ and $\vec{x}_{s'}$ are on the surface S.

Equation (6.25) is known as the surface Helmholtz integral equation because there is an unknown variable under the integral sign. Once the surface acoustic pressure $\hat{p}\left(\vec{x}_s;\omega\right)$ and normal surface velocity $\hat{v}_{\mathrm{n}}\left(\vec{x}_s;\omega\right)$ are specified, the acoustic pressure $\hat{p}\left(\vec{x};\omega\right)$ in free space is completely determined by Eq. (6.10). The complexities of the problem are significantly reduced because one only deals with discretization of a two-dimensional source surface. The trouble is that Eq. (6.25) may fail to produce a unique solution whenever the frequency is equal to 1 of the characteristic frequencies of the corresponding boundary value problem in the interior region.

6.2 Nonuniqueness Difficulties

The nonuniqueness difficulties of the surface Helmholtz integral equation (6.25) can be examined by looking at a general Fredholm integral equation of the second kind [96],

$$u(\varsigma) - \Lambda\iint_S K(\varsigma,\xi)u(\xi)dS(\xi) = F(\varsigma), \tag{6.26}$$

where $u(\varsigma)$ is unknown, $K(\varsigma, \xi)$ is called "L^2 kernels," meaning that they are square integrable over S in the Lebesgue sense, Λ is some value whose meaning will be specified shortly, and $F(\varsigma)$ is a known function. The associate homogeneous Fredholm integral equation is given by

$$u_0(\varsigma) - \Lambda \iint_S K(\varsigma, \xi) u_0(\xi) dS(\xi) = 0. \tag{6.27}$$

The Sturm-Liouville theory [97] states that if the associated homogeneous equation (6.27) has a nontrivial solution $u_0(\varsigma)$, then Λ is a characteristic value or eigenvalue of the kernel $K(\varsigma, \xi)$ and $u_0(\varsigma)$ is a characteristic function of $K(\varsigma, \xi)$ belonging to Λ. Otherwise Λ is a regular value.

The adjoint inhomogeneous Fredholm integral equation of the second kind is expressible as

$$y(\varsigma) - \Lambda^* \iint_S K(\varsigma, \xi)^* y(\xi) dS(\xi) = H(\varsigma), \tag{6.28}$$

where $K(\varsigma, \xi)^*$ is the adjoint kernel of $K(\varsigma, \xi)$ and $H(\varsigma)$ is given. The adjoint homogeneous equation for Eq. (6.28) is

$$y_0(\varsigma) - \Lambda^* \iint_S K(\varsigma, \xi)^* y_0(\xi) dS(\xi) = 0. \tag{6.29}$$

The following theorems have been proven by Smithies [97]

Theorem 6.1 *If Λ is a regular value of $K(\varsigma, \xi)$, then Λ^* is a regular value of $K(\varsigma, \xi)^*$, the homogeneous Eqs. (6.27) and (6.29) have only trivial solutions, and Eqs. (6.26) and (6.28) have unique solutions for any L^2 functions $F(\varsigma)$ and $H(\varsigma)$.*

Theorem 6.2 *If Λ is a characteristic value of $K(\varsigma, \xi)$, then Λ^* is a characteristic value of $K(\varsigma, \xi)^*$, and the homogeneous Eqs. (6.27) and (6.29) have nontrivial solutions.*

Theorem 6.3 *If Λ is a characteristic value of $K(\varsigma, \xi)$, then the inhomogeneous equation (6.27) has an L^2 solution if and only if $F(\varsigma)$ is orthogonal to every L^2 solution of the adjoint homogeneous equation (6.29), i.e., if $F(\varsigma)$ satisfies*

$$\iint_S y_0(\xi)^* F(\xi) dS(\xi) = 0. \tag{6.30}$$

Furthermore, even if the compatibility condition (6.30) is satisfied, the solution to Eq. (6.26) is not determined uniquely since any multiple of $u_0(\varsigma)$ can be added to a particular solution of Eq. (6.26).

Now let us apply these theorems to examining the solution of the surface Helmholtz integral equation (6.25). Let

$$u(\varsigma) = \hat{p}\left(\vec{x}_s;\omega\right), K(\varsigma,\xi) = \frac{1}{2\pi}\frac{\partial G\left(\vec{x}_s\middle|\vec{x}_{s'};\omega\right)}{\partial \mathrm{n}\left(\vec{x}_{s'}\right)}, \Lambda = 1, \quad \text{and}$$
$$F(\varsigma) = -\frac{i\omega\rho_0}{2\pi}\iint\limits_S \hat{v}_{\mathrm{n}}\left(\vec{x}_{s'};\omega\right)G\left(\vec{x}_s\middle|\vec{x}_{s'};\omega\right)dS'. \tag{6.31}$$

Substituting Eq. (6.31) into Eq. (6.26), we obtain

$$\hat{p}\left(\vec{x}_s;\omega\right) - \frac{1}{2\pi}\iint\limits_{S'} \hat{p}\left(\vec{x}_{s'};\omega\right)\frac{\partial G\left(\vec{x}_s\middle|\vec{x}_{s'};\omega\right)}{\partial \mathrm{n}\left(\vec{x}_{s'}\right)}dS'$$
$$= -\frac{i\omega\rho_0}{2\pi}\iint\limits_S \hat{v}_{\mathrm{n}}\left(\vec{x}_{s'};\omega\right)G\left(\vec{x}_s\middle|\vec{x}_{s'};\omega\right)dS', \tag{6.32}$$

where $\hat{v}_{\mathrm{n}}\left(\vec{x}_s;\omega\right)$ is specified, and $\hat{p}\left(\vec{x}_S;\omega\right)$ is to be determined. The corresponding homogeneous equation is given by

$$\hat{p}\left(\vec{x}_s;\omega\right) - \frac{1}{2\pi}\iint\limits_{S'} \hat{p}\left(\vec{x}_{s'};\omega\right)\frac{\partial G\left(\vec{x}_s\middle|\vec{x}_{s'};\omega\right)}{\partial \mathrm{n}\left(\vec{x}_{s'}\right)}dS' = 0. \tag{6.33}$$

From Theorems 6.1 and 6.2 we know that Eq. (6.32) has a unique solution, except at some characteristic frequencies for which Eq. (6.33) has nontrivial solutions.

From Theorem 6.3 we further learn that at these characteristic frequencies, Eq. (6.33) has no solution unless the compatibility condition [see Eq. (6.30)],

$$-\frac{i\omega\rho_0}{2\pi}\iint\limits_S \hat{p}_0\left(\vec{x}_s;\omega\right)^*\left[\iint\limits_{S'} \hat{v}_{\mathrm{n}}\left(\vec{x}_{s'};\omega\right)G\left(\vec{x}_s\middle|\vec{x}_{s'};\omega\right)dS'\right]dS = 0, \tag{6.34}$$

holds for all $\hat{p}_0\left(\vec{x}_s;\omega\right)^*$, which satisfies the adjoint homogeneous equation (6.29),

$$\hat{p}_0\left(\vec{x}_s;\omega\right)^* - \frac{1}{2\pi}\iint\limits_{S'} \hat{p}_0\left(\vec{x}_{s'};\omega\right)^*\frac{\partial G\left(\vec{x}_s\middle|\vec{x}_{s'};\omega\right)}{\partial \mathrm{n}\left(\vec{x}_{s'}\right)}dS' = 0. \tag{6.35}$$

To show that compatibility condition (6.30) is satisfied, we consider the interior problem, for which the Helmholtz integral formulation can be written as

$$\hat{p}^{\mathrm{I}}\left(\vec{x};\omega\right) = -\frac{1}{4\pi}\iint\limits_{S'}\hat{p}^{\mathrm{I}}\left(\vec{x}_{s'};\omega\right)\frac{\partial G\left(\vec{x}\middle|\vec{x}_{s'};\omega\right)}{\partial \mathrm{n}\left(\vec{x}_{s'}\right)}dS' + \frac{i\omega\rho_0}{4\pi}\iint\limits_{S'}\hat{v}_{\mathrm{n}}^{\mathrm{I}}\left(\vec{x}_{s'};\omega\right)G\left(\vec{x}\middle|\vec{x}_{s'};\omega\right)dS. \tag{6.36}$$

Note that Eq. (6.36) can be derived in the same way as that of Eq. (6.10), except that the sign of the unit normal on the surface should be reversed for the interior problem.

Taking the limit as the field point approaches the surface from the inside, we obtain

$$\hat{p}^{\mathrm{I}}\left(\vec{x}_{\mathrm{s}};\omega\right) + \frac{1}{2\pi}\iint\limits_{S'}\hat{p}^{\mathrm{I}}\left(\vec{x}_{\mathrm{s}'};\omega\right)\frac{\partial G\left(\vec{x}_{\mathrm{s}}\middle|\vec{x}_{\mathrm{s}'};\omega\right)}{\partial \mathrm{n}\left(\vec{x}_{\mathrm{s}'}\right)}dS' = \frac{i\omega\rho_0}{2\pi}\iint\limits_{S'}\hat{v}_{\mathrm{n}}^{\mathrm{I}}\left(\vec{x}_{\mathrm{s}'};\omega\right)G\left(\vec{x}_{\mathrm{s}}\middle|\vec{x}_{\mathrm{s}'};\omega\right)dS'. \tag{6.37}$$

On the other hand, taking the normal derivative of the Helmholtz integral formulation for the interior region, Eq. (6.36), we obtain

$$i\omega\rho_0\hat{v}_{\mathrm{n}}^{\mathrm{I}}\left(\vec{x};\omega\right) = -\frac{1}{4\pi}\frac{\partial}{\partial \mathrm{n}}\iint\limits_{S'}\hat{p}^{\mathrm{I}}\left(\vec{x}_{s'};\omega\right)\frac{\partial G\left(\vec{x}\middle|\vec{x}_{s'};\omega\right)}{\partial \mathrm{n}\left(\vec{x}_{s'}\right)}dS' + \frac{i\omega\rho_0}{4\pi}\iint\limits_{S'}\hat{v}_{\mathrm{n}}^{\mathrm{I}}\left(\vec{x}_{s'};\omega\right)\frac{\partial G\left(\vec{x}\middle|\vec{x}_{s'};\omega\right)}{\partial \mathrm{n}\left(\vec{x}_{s'}\right)}dS'. \tag{6.38}$$

Taking the limit as $\vec{x} \to \vec{x}_s$ from the inside yields

$$i\omega\rho_0\hat{v}_{\mathrm{n}}^{\mathrm{I}}\left(\vec{x}_s;\omega\right) - \frac{i\omega\rho_0}{2\pi}\iint\limits_{S'}\hat{v}_{\mathrm{n}}^{\mathrm{I}}\left(\vec{x}_{s'};\omega\right)\frac{\partial G\left(\vec{x}_s\middle|\vec{x}_{s'};\omega\right)}{\partial \mathrm{n}\left(\vec{x}_{s'}\right)}dS' = -\frac{1}{2\pi}\frac{\partial}{\partial \mathrm{n}}\iint\limits_{S'}\hat{p}^{\mathrm{I}}\left(\vec{x}_{s'};\omega\right)\frac{\partial G\left(\vec{x}_s\middle|\vec{x}_{s'};\omega\right)}{\partial \mathrm{n}\left(\vec{x}_{s'}\right)}dS'. \tag{6.39}$$

For the Dirichlet problem for which $\hat{p}^{\mathrm{I}}\left(\vec{x}_s;\omega\right) = 0$ on the source surface, Eq. (6.39) reduces to

$$i\omega\rho_0 \hat{v}_{\mathrm{n}}^{\mathrm{I}}\left(\vec{x}_s;\omega\right) - \frac{i\omega\rho_0}{2\pi}\iint\limits_{S'} \hat{v}_{\mathrm{n}}^{\mathrm{I}}\left(\vec{x}_{s'};\omega\right)\frac{\partial G\left(\vec{x}_s\middle|\vec{x}_{s'};\omega\right)}{\partial \mathrm{n}\left(\vec{x}_{s'}\right)}dS' = 0. \tag{6.40}$$

The roots of this homogeneous equation are called the Dirichlet eigenfrequencies, $k = k_{\mathrm{D}}$. At these characteristic frequencies Eq. (6.40) has nontrivial solutions that are known as the characteristic functions belonging to the characteristic frequencies k_{D}.

Note that Eq. (6.40) has the same form as the homogeneous surface Helmholtz integral equation (6.33). Accordingly, they share the same characteristic frequencies k_{D}. In other words, the set of solutions $\hat{v}_{\mathrm{n}}^{\mathrm{I}}\left(\vec{x}_s;\omega\right)$ for the interior Dirichlet problem are the same as those of $\hat{p}\left(\vec{x}_s;\omega\right)$ for the exterior Neumann problem for which $\hat{v}_{\mathrm{n}}\left(\vec{x}_s;\omega\right) = 0$ on the surface. In fact, applying this Neumann boundary condition in Eq. (6.32), we obtain Eq. (6.33), which has the same form as that of Eq. (6.40).

Now applying the Dirichlet boundary condition to the interior Helmholtz integral equation (6.37), we obtain

$$\iint\limits_{S'} \hat{v}_{\mathrm{n}}^{\mathrm{I}}\left(\vec{x}_{s'};\omega\right) G\left(\vec{x}_s\middle|\vec{x}_{s'};\omega\right)dS' = 0. \tag{6.41}$$

Because of the equivalence of solutions sets $\hat{v}_{\mathrm{n}}^{\mathrm{I}}\left(\vec{x}_s;\omega\right)$ for the interior region and $\hat{p}\left(\vec{x}_s;\omega\right)$ for the exterior region, we can interchange these two sets and rewrite Eq. (6.41) as

$$\iint\limits_{S'} \hat{p}\left(\vec{x}_{s'};\omega\right) G\left(\vec{x}_s\middle|\vec{x}_{s'};\omega\right)dS' = 0 \quad \text{or} \quad \iint\limits_{S'} \hat{p}\left(\vec{x}_{s'};\omega\right)^* G\left(\vec{x}_s\middle|\vec{x}_{s'};\omega\right)dS' = 0. \tag{6.42}$$

Substituting Eq. (6.42) into Eq. (6.34) and interchanging the order of integrations, we obtain

$$\begin{aligned} &-\frac{i\omega\rho_0}{2\pi}\iint\limits_{S} \hat{p}_0\left(\vec{x}_s;\omega\right)^*\left[\iint\limits_{S'} \hat{v}_{\mathrm{n}}\left(\vec{x}_{s'};\omega\right) G\left(\vec{x}_s\middle|\vec{x}_{s'};\omega\right)dS'\right]dS \\ &= -\frac{i\omega\rho_0}{2\pi}\iint\limits_{S} \hat{v}_{\mathrm{n}}\left(\vec{x}_s;\omega\right)\left[\iint\limits_{S'} \hat{p}_0\left(\vec{x}_{s'};\omega\right)^* G\left(\vec{x}_s\middle|\vec{x}_{s'};\omega\right)dS'\right]dS \equiv 0. \end{aligned} \tag{6.43}$$

Equation (6.43) shows that the compatibility condition is perfectly satisfied and Eq. (6.33) has nontrivial solution. However, the solution to the surface Helmholtz integral equation (6.32) may be nonunique because any multiple of $\hat{v}_{\mathrm{n}}\left(\vec{x}_s;\omega\right)$ may be added to the particular solution and the compatibility condition (6.43) is still satisfied.

Therefore the surface Helmholtz integral equation (6.25) fails to yield a unique solution whenever the frequency coincides with one of the characteristic values for the interior Dirichlet boundary value problem. However, among all these characteristic frequencies there is only one set that also satisfies the interior Helmholtz integral formulation simultaneously. This is the basis for the Combined Helmholtz Integral Equation Formulation or CHIEF for short that provides unique solutions for acoustic radiation problems at any frequency.

6.3 Discrete Helmholtz Integral Formulations

For arbitrarily shaped surfaces, the Helmholtz integral formulation (6.10) and the surface Helmholtz integral equation (6.25) cannot be solved analytically. Hence numerical solutions are sought. Suppose that the surface is discretized into segments with N nodes, then Eqs. (6.10) and (6.25) can be rewritten as

$$\hat{p}\left(\vec{x};\omega\right) = \left\{T_p\left(\vec{x}\middle|\vec{x}_s;\omega\right)\right\}_{1\times N}\left\{\hat{p}\left(\vec{x}_s;\omega\right)\right\}_{N\times 1}, \tag{6.44}$$

$$\hat{p}\left(\vec{x};\omega\right) = \left\{T_v\left(\vec{x}\middle|\vec{x}_s;\omega\right)\right\}_{1\times N}\left\{\hat{v}_{\mathrm{n}}\left(\vec{x}_s;\omega\right)\right\}_{N\times 1}, \tag{6.45}$$

where $\left\{T_p\left(\vec{x}\middle|\vec{x}_s;\omega\right)\right\}_{1\times N}$ and $\left\{T_v\left(\vec{x}\middle|\vec{x}_s;\omega\right)\right\}_{1\times N}$ represent, respectively, the transfer functions that correlate the surface acoustic pressure and normal surface velocity to the field acoustic pressure, and are given by

$$\left\{T_p\left(\vec{x}\middle|\vec{x}_s;\omega\right)\right\}_{1\times N} = (4\pi)^{-1}\left(\{D\}_{1\times N} + \{M\}_{1\times N}[M_s]^{-1}_{N\times N}\left(2\pi[\mathrm{I}]_{N\times N} - [D_s]_{N\times N}\right)\right), \tag{6.46}$$

$$\left\{T_v\left(\vec{x}\middle|\vec{x}_s;\omega\right)\right\}_{1\times N} = (4\pi)^{-1}\left(\{D\}_{1\times N}\left(2\pi[\mathrm{I}]_{N\times N} - [D_s]_{N\times N}\right)^{-1}[M_s]_{N\times N} + \{M\}_{1\times N}\right), \tag{6.47}$$

where $[\mathrm{I}]_{N\times N}$ is a unitary matrix, $[M_s]_{N\times N}$ and $[D_s]_{N\times N}$ depict the effects of monopoles and dipoles on a surface point, respectively, and $[M]_{N\times N}$ and $[D]_{N\times N}$ describe those of monopoles and dipoles on a field point, respectively. The $\mu\nu$th elements of these matrices are given by

$$M_{\mu\nu} = G\left(\vec{x}_{\mu}\middle|\vec{x}_{s',\nu};\omega\right)J_{\mu\nu} \quad \text{and} \quad D_{\mu\nu} = \frac{\partial G\left(\vec{x}_{\mu}\middle|\vec{x}_{s',\nu};\omega\right)}{\partial \mathrm{n}\left(\vec{x}_{s'}\right)}J_{\mu\nu}, \tag{6.48}$$

$$M_{s,\mu\nu} = G\left(\vec{x}_{s,\mu}\middle|\vec{x}_{s',\nu};\omega\right)J_{\mu\nu} \quad \text{and} \quad D_{s,\mu\nu} = \frac{\partial G\left(\vec{x}_{s,\mu}\middle|\vec{x}_{s',\nu};\omega\right)}{\partial \mathrm{n}\left(\vec{x}_{s'}\right)}J_{\mu\nu}, \tag{6.49}$$

where $J_{\mu\nu}$ indicates the Jacobian of the surface integration in Eqs. (6.46) and (6.47) [98].

In the BEM-based NAH, the goal is to reconstruct the surface acoustic quantities based on discrete N nodes. So we need to take at least N measurement points of the field acoustic pressures to form a square matrix in Eqs. (6.44) and (6.45). Accordingly, we can rewrite Eqs. (6.44) and (6.45) as

$$\left\{\hat{p}\left(\vec{x}_{m};\omega\right)\right\}_{N\times 1} = \left[T_p\left(\vec{x}\middle|\vec{x}_{s};\omega\right)\right]_{N\times N}\left\{\hat{p}\left(\vec{x}_{s};\omega\right)\right\}_{N\times 1}, \tag{6.50}$$

$$\left\{\hat{p}\left(\vec{x}_{m};\omega\right)\right\}_{N\times 1} = \left[T_v\left(\vec{x}\middle|\vec{x}_{s};\omega\right)\right]_{N\times N}\left\{\hat{v}_{\mathrm{n}}\left(\vec{x}_{s},\omega\right)\right\}_{N\times 1}, \tag{6.51}$$

where $\hat{p}\left(\vec{x}_{m};\omega\right)$, $m = 1$ to N, represent the measured acoustic pressures.

Equations (6.50) and (6.51) enables one to reconstruct surface acoustic pressure $\hat{p}\left(\vec{x}_{s};\omega\right)$ and normal surface velocity $\hat{v}_{\mathrm{n}}\left(\vec{x}_{s};\omega\right)$ through inversion of matrices $\left[T_p\left(\vec{x}\middle|\vec{x}_{s};\omega\right)\right]_{N\times N}$ and $\left[T_v\left(\vec{x}\middle|\vec{x}_{s};\omega\right)\right]_{N\times N}$, respectively. In practice, the measured acoustic pressures $\hat{p}\left(\vec{x}_{m};\omega\right)$ are not error free. As a result, the matrix equations (6.50) and (6.51) may be ill conditioned. To overcome this difficulty, regularization can be employed, the simplest one being a TSVD to eliminate the evanescent waves that fall below the background noise level. Accordingly, $\hat{p}\left(\vec{x}_{s};\omega\right)$ and $\hat{v}_{\mathrm{n}}\left(\vec{x}_{s};\omega\right)$ can be written as

$$\left\{\hat{p}\left(\vec{x}_{s};\omega\right)\right\}_{N\times 1} = \left[V_p\right]_{N\times N}\left[\Sigma_p^{-1}\right]_{N\times N}\left[U_p\right]_{N\times N}^{\mathrm{T}}\left\{\hat{p}\left(\vec{x}_{m},\omega\right)\right\}_{N\times 1}, \tag{6.52}$$

$$\left\{\hat{v}_{\mathrm{n}}\left(\vec{x}_{s};\omega\right)\right\}_{N\times 1} = \left[V_v\right]_{N\times N}\left[\Sigma_v^{-1}\right]_{N\times N}\left[U_v\right]_{N\times N}^{\mathrm{T}}\left\{\hat{p}\left(\vec{x}_{m},\omega\right)\right\}_{N\times 1}, \tag{6.53}$$

where $[V_p]_{N\times N}$ and $[U_p]_{N\times N}$, respectively, are the right and left unitary matrices of the transfer matrix $\left[T_p\left(\vec{x}\middle|\vec{x}_{s};\omega\right)\right]_{N\times N}$, namely, they satisfy $[V_p]_{N\times N}[V_p]_{N\times N}^{\mathrm{T}} = [\mathrm{I}]_{N\times N}$ and $[U_p]_{N\times N}[U_p]_{N\times N}^{\mathrm{T}} = [\mathrm{I}]_{N\times N}$, and $[\Sigma_p]^{-1} = \mathrm{diag}[\ldots, 1/\sigma_{p,n}, \ldots]$ stands for the diagonal matrix containing inversions of the non-zero singularities $\sigma_{p,n}$ of the matrix $\left[T_p\left(\vec{x}\middle|\vec{x}_{s};\omega\right)\right]_{N\times N}$. Similarly, $[V_v]_{N\times N}$ and $[U_v]_{N\times N}$ are the right and left unitary matrices of the transfer matrix $\left[T_v\left(\vec{x}\middle|\vec{x}_s;\omega\right)\right]_{N\times N}$, respectively, $[V_v]_{N\times N}[V_v]^{\mathrm{T}}_{N\times N}=[\mathrm{I}]_{N\times N}$ and $[U_v]_{N\times N}[U_v]^{\mathrm{T}}_{N\times N}=[\mathrm{I}]_{N\times N}$, and $[\Sigma_v]^{-1}=\mathrm{diag}\,[\ldots,1/\sigma_{v,n},\ldots]$ is the diagonal matrix that contains inversions of the non-zero singularities $\sigma_{v,n}$ of the matrix $\left[T_v\left(\vec{x}\middle|\vec{x}_s;\omega\right)\right]_{N\times N}$.

Equations (6.52) and (6.53) gives the reconstructed acoustic quantities on the surface of any arbitrary structure. A rule of thumb in discretization for the BEM method is to have a minimum of six nodes per wavelength. For a complex structure vibrating at mid-to-high frequencies, the total number of discrete nodes needed to depict the surface acoustic quantities can be extremely large. As a result, the number of measurements required to reconstruct the acoustic quantities can be very high, thus making the reconstruction process unrealistically time consuming.

6.4 The Combined Helmholtz Equation Least-Squares Method

To enhance the efficiency of the BEM-based NAH and improve the accuracy of the HELS method for reconstructing the acoustic field generated by an arbitrary structure, we combine these two methods and describe the procedures as follows:

1. Take the acoustic pressures $\hat{p}\left(\vec{x}_m^{\,\mathrm{meas}};\omega\right)$, $m=1$ to M, on the hypothetical spherical surface that encloses the target source surface.
2. Divide the measurement points into two groups M_1 and M_2, where $M=M_1+M_2$.
3. Use M_1 as the input to establish the HELS formulations to reconstruct the acoustic pressure on M_2 points on the measurement surface,

$$\left\{\hat{p}\left(\vec{x}_m^{\,\mathrm{rec}};\omega\right)\right\}_{M_2\times 1}=\left[G_{pp}\left(\vec{x}_m^{\,\mathrm{rec}}\middle|\vec{x}_m^{\,\mathrm{meas}};\omega\right)\right]_{M_2\times M_1}\left\{\hat{p}\left(\vec{x}_m^{\,\mathrm{meas}};\omega\right)\right\}_{M_1\times 1},\tag{6.54}$$

where $\left[G_{pp}\left(\vec{x}_m^{\,\mathrm{rec}}\middle|\vec{x}_m^{\,\mathrm{meas}};\omega\right)\right]_{N\times M_1}$ is defined in Eq. (3.16).

Note that since the least-squares method is used, the expansion solution (6.54) with $J=M_1$ will be the best fit at M_1 measurement locations, but it may not be the best approximation for the remaining M_2 values. This is especially true when the measured acoustic pressures contain errors. Consequently, the accuracy in reconstruction at M_2 locations will increase with J first, and then deteriorates thereafter.

4. Find the optimal expansion term J_{op}, which is equivalent to finding a low-pass filter for the spherical harmonics such that the evanescent waves below the background noise level are eliminated. There are many regularization techniques available for solving a set of linear equations. The simplest yet very effective for the HELS method is an iteration scheme,

$$\min_{J} \sum_{i=1}^{M} \left|\left| \hat{p}\left(\vec{x}_{m,i}^{\,\text{rec}}; \omega\right) - \hat{p}\left(\vec{x}_{m,i}^{\,\text{meas}}; \omega\right) \right|\right|_2^2 \rightarrow J_{\text{op}}, \tag{6.55}$$

where reconstruction is done on the measurement surface to determine the value of J_{op}.

5. Use J_{op} in Eq. (6.55) to regenerate the acoustic pressures at as many points as necessary on the measurement surface, say, the same as that of discrete notes,

$$\left\{\hat{p}\left(\vec{x}_m^{\,\text{rec}}; \omega\right)\right\}_{N\times 1} = \left[G_{pp}\left(\vec{x}_m^{\,\text{rec}} \middle| \vec{x}_m^{\,\text{meas}}; \omega\right)\right]_{N\times M_1} \left\{\hat{p}\left(\vec{x}_m^{\,\text{meas}}; \omega\right)\right\}_{M_1\times 1}. \tag{6.56}$$

6. Take these regenerated acoustic pressures $\hat{p}\left(\vec{x}_m^{\,\text{rec}}; \omega\right)$ as input data to the BEM-based NAH formulations to reconstruct the acoustic pressure $\hat{p}\left(\vec{x}_s^{\,\text{rec}}; \omega\right)$ and normal velocity $\hat{v}_{\text{n}}\left(\vec{x}_s^{\,\text{rec}}; \omega\right)$ on the source surface,

$$\begin{aligned} &\left\{\hat{p}\left(\vec{x}_s^{\,\text{rec}}; \omega\right)\right\}_{N\times 1} \\ &= \left[V_p\right]_{N\times N} \left[\Sigma_p^{-1}\right]_{N\times N} \left[U_p\right]_{N\times N}^{\text{T}} \left[G_{pp}\left(\vec{x}_m^{\,\text{rec}} \middle| \vec{x}_m^{\,\text{meas}}; \omega\right)\right]_{N\times M_1} \left\{\hat{p}\left(\vec{x}_m^{\,\text{meas}}; \omega\right)\right\}_{M_1\times 1}, \end{aligned} \tag{6.57}$$

$$\begin{aligned} &\left\{\hat{v}_{\text{n}}\left(\vec{x}_s^{\,\text{rec}}; \omega\right)\right\}_{N\times 1} \\ &= \left[V_v\right]_{N\times N} \left[\Sigma_v^{-1}\right]_{N\times N} \left[U_v\right]_{N\times N}^{\text{T}} \left[G_{pp}\left(\vec{x}_m^{\,\text{rec}} \middle| \vec{x}_m^{\,\text{meas}}; \omega\right)\right]_{N\times M_1} \left\{\hat{p}\left(\vec{x}_m^{\,\text{meas}}; \omega\right)\right\}_{M_1\times 1}, \end{aligned} \tag{6.58}$$

where the matrix $\left[G_{pp}\left(\vec{x}_m^{\,\text{rec}} \middle| \vec{x}_m^{\,\text{meas}}; \omega\right)\right]_{N\times M_1}$ is given, respectively, by

$$\begin{aligned} &\left[G_{pp}\left(\vec{x}_m^{\,\text{rec}} \middle| \vec{x}_m^{\,\text{meas}}; \omega\right)\right]_{N\times M_1} \\ &= \left[\Psi\left(\vec{x}_m^{\,\text{rec}}; \omega\right)\right]_{N\times J_{\text{op}}} \left(\left[\Psi\left(\vec{x}_m^{\,\text{meas}}; \omega\right)\right]_{J_{\text{op}}\times M_1}^{H} \left[\Psi\left(\vec{x}_m^{\,\text{meas}}; \omega\right)\right]_{M_1\times J_{\text{op}}}\right)^{-1} \\ &\quad \left[\Psi\left(\vec{x}_m^{\,\text{meas}}; \omega\right)\right]_{J_{\text{op}}\times M_1}^{H}, \end{aligned} \tag{6.59}$$

where the elements of $\left[\Psi\left(\vec{x}_m^{\,\text{meas}}; \omega\right)\right]_{M_1\times J_{\text{op}}}$ are given in Eq. (3.2).

The enhancement in the reconstruction efficiency is obvious. Equation (6.59) shows that $\hat{p}\left(\vec{x}_s^{\,\mathrm{rec}}, \omega\right)$ and $\hat{v}_{\mathrm{n}}\left(\vec{x}_s^{\,\mathrm{rec}}, \omega\right)$ on N nodes of the arbitrarily shaped surface can now be reconstructed using M_1 measurements. Since $M << N$, the required measurement time is significantly reduced.

Note that the accuracy of the regenerated field acoustic pressure is consistent with that of measured data for $\vec{x}_m \in \vec{X}$. This is because the acoustic pressure for $\vec{x}_m \in \vec{X}$ can be completely and uniquely described by Eq. (6.54) as $J \to \infty$. The omission of the higher-order terms, namely, the evanescent waves have a negligibly small impact on the resultant field acoustic pressure. Hence, there is no need to take more measurements than necessary. In fact, the accuracy of reconstruction would remain unchanged, even if the regenerated field acoustic pressures were replaced by the real measurements. The trade-off is that the accuracy in reconstruction may be limited because certain evanescent waves have been lost as measurements are taken over a spherical surface rather than a conformal surface at close range.

It is emphasized that one cannot extend the processes discussed above to the region inside the minimum sphere, either by taking measurements or regenerating the acoustic pressures. This is because the acoustic pressure there cannot be represented adequately by the spherical waves.

6.5 Applications of the CHELS Method

In this section we examine the performance of the CHELS method and compare its results with that of the BEM-based NAH. In particular, we want to check if CHELS can yield satisfactory reconstruction of an acoustic field accurately and efficiently based on greatly reduced input data.

Example 6.1 Consider a partially vibrating sphere of radius $a = 0.1$ m. The reason for selecting this example is because it contains very rich evanescent waves and yet the analytic solution is readily available. The normal surface velocity distribution $\hat{v}_{\mathrm{n}}$ can be written as

$$\hat{v}_{\mathrm{n}}(a, \theta, \varphi; \omega) = \begin{cases} v_0, & 0 \le |\theta| \le \theta_0 \\ 0, & \text{otherwise} \end{cases}, \tag{6.60}$$

where v_0 is a constant and the half vertex angle is, say, $\angle\theta_0 = 36°$.

Since the source is a sphere, the minimum surface is spherical. Following the guidelines as given in Chap. 5, we gauge the measurement distance d and microphone spacing δ with respect to the critical spatial wavelength λ_{cr}. Suppose that as an initial guess, we set $\lambda_{\mathrm{cr}} = a/3$ and $\delta < \lambda_{\mathrm{cr}}/2$. Since $a = 0.1$ m, we find $\lambda_{\mathrm{cr}} \approx 0.033$ m and $\delta = 0.0165$ m. The number of measurement points can be estimated by using Eq. (5.3). Since the source surface $S = 2\pi a^2$, $a = 0.1$ m, and $\lambda_{cr} \approx 0.033$ m, we have $M > 4 \times (2\pi \times 0.1^2)/0.033^2 \approx 278$. All the input acoustic pressures are calculated by using the formulation given by Morse and Ingard [99], of which $M_1 = 76$ are used in Eq. (6.56) to regenerate the acoustic pressures on the spherical measurement surface and the rest $M_2 = 202$ points are used to optimize the number of expansion functions J_{op}. In this case $J_{op} = 26$ is found to be acceptable for $0 < ka \leq 10$. The regenerated field acoustic pressures are taken as input to Eqs. (6.57) and (6.58).

Note that for any given set of measurements in engineering practice, a larger value of J_{op} indicates an inclusion of more evanescent waves and the higher the accuracy of reconstruction can be. A smaller value of J_{op} implies a lower SNR and less evanescent waves included in input data. As a result, the reconstructed acoustic field may be unsatisfactory.

For comparison, we use the BEM-based NAH to reconstruct the surface acoustic quantities. To ensure the accuracy in reconstruction, we use six discrete nodes per structural wavelength to depict the surface acoustic quantities. Suppose that we take six discrete nodes per critical spatial wavelength, $\delta = \lambda_{cr}/6$. Since $\lambda_{cr} \approx 0.033$ m, we have $\delta = 0.0055$ m, which leads to a total number of $N = 602$ discrete nodes. Accordingly, we need to take $M = 602$ measurement points of the acoustic pressures, which are obtained by using the formulation given by Morse and Ingard [99] and taken as input to the BEM-based NAH Eqs. (6.52) and (6.53) to reconstruct the surface acoustic pressure and normal component of the surface velocity.

In this example, we show the reconstruction results based on a coarse mesh with an average distance between neighboring discrete nodes $\delta = 0.032$ m, which is twice the value of $\delta = 0.0165$ m as suggested for CHELS. Accordingly, the number of nodes by using a triangular element and the first-order interpolation is reduced to $N = 152$. The number of measurement points is the same as that of the discrete nodes, i.e., $M = 152$.

Figure 6.2 shows the comparison of the reconstructed acoustic pressures at $ka = 1.46$ on the generator of the sphere. Results show that the surface acoustic pressures reconstructed by CHELS with $N = 152$ agree very well with those of the BEM codes with $N = 602$ and the analytic solutions.

While a fine mesh does not make much difference in reconstructing the acoustic pressure, it does have a significant impact on reconstructing the normal surface velocity. Figure 6.3 shows that a coarse mesh with $N = 152$ nodes only enables one to capture the main characteristics of the normal surface velocity distribution. By using a fine mesh of $N = 602$ nodes and the same number of the input data points regenerated by Eq. (6.56), we can significantly improve the reconstruction accuracy. This is because the surface normal velocity distribution has a sharp edge that contains higher wavenumber contents than the surface acoustic pressure does.

The fact that the CHELS method can yield satisfactory reconstruction with relatively few measurements is of a great significance. It indicates that the fidelity of the input data regenerated by Eq. (6.56) is preserved. Hence, one does not need to take more measurements than necessary. Moreover, it shows that one can improve

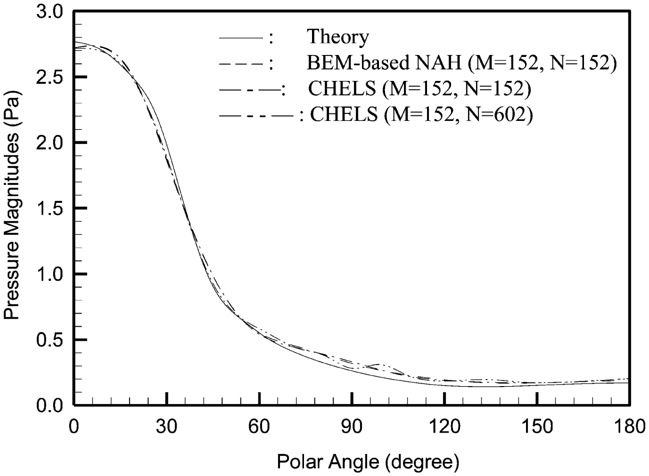

Fig. 6.2 Comparison of the reconstructed acoustic pressure distributions on the surface of a partially vibrating sphere at $ka = 1.46$ based on measurements taken at $r = 0.105$ m

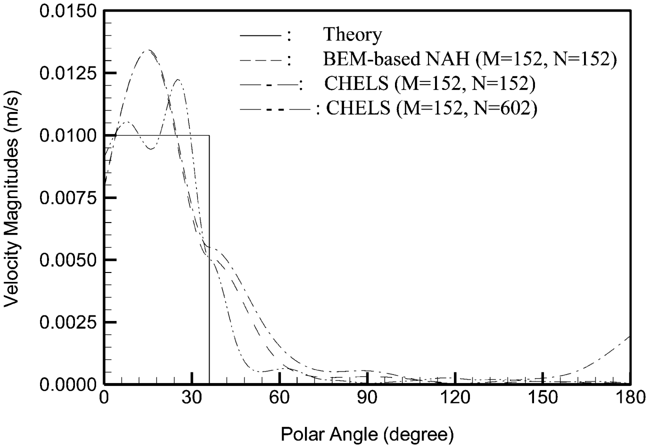

Fig. 6.3 Comparison of reconstructed normal component of velocity distributions on the surface of a partially vibrating sphere at $ka = 1.46$ based on measurements taken at $r = 0.105$ m

the accuracy by increasing the input data. Because these data are calculated but not measured, the efficiency of reconstruction is significantly enhanced.

However, one should not expect the normal surface velocity to converge to the true value even as the number of regenerated input data approaches infinity. This is because the accuracy of reconstruction is controlled by the amount of evanescent waves captured in the measured data. The closer the measurements are to the source surface, the more the evanescent waves are captured, and the more accurate the

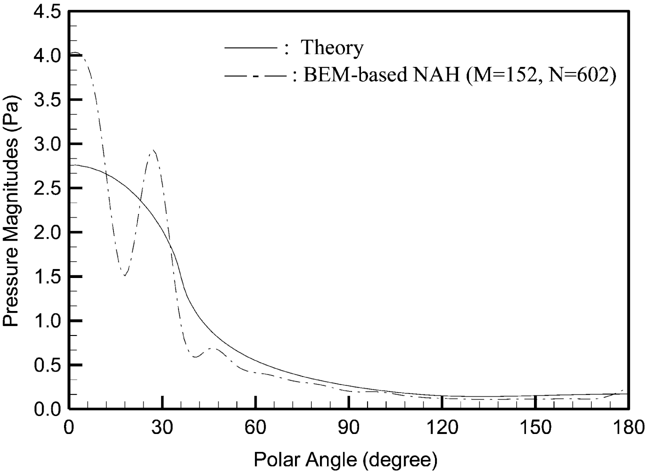

Fig. 6.4 Reconstructed acoustic pressure distribution on the surface of a partially vibrating sphere at $ka = 1.46$ using the BEM-based NAH with 602 discrete nodes and 152 measurements taken at $r = 0.105$ m

reconstruction is. Once the measurement distance is fixed, so is the amount of the evanescent waves that can be captured. Thus the improvement in the reconstruction accuracy through increasing the number of regenerated input data is limited.

Also, it is emphasized that we do not need to have exactly the same measurement number as the discrete nodes. This is because using SVD and regularization, we can have either an over- or under-determined system of equations, or equivalently, take more or fewer measurements than the discrete nodes. However, if the measurements are too few, a spatial aliasing may occur and the resulting reconstruction can be greatly distorted. Figure 6.4 displays that when 152 field acoustic pressures are taken as the input to the BEM-based NAH for a surface with 602 discrete nodes, the resulting reconstruction of the surface acoustic pressure is severely distorted.

To show the effect of measurement distances on the reconstruction accuracy, we present the reconstructed surface acoustic quantities based on conformal measurements taken at different radial distances $r = 0.105$, 0.110, 0.125, and 0.150 m under $ka = 1.46$. Figure 6.5 depicts that as measurement distances increase, more and more evanescent waves are lost in the input data. As a result, the reconstructed normal surface velocity becomes more and more distorted. However the accuracy in reconstruction of the surface acoustic pressure remains essentially unchanged (results omitted for brevity). This is because the normal surface velocity contains more near-field effects than the surface acoustic pressure does. These results demonstrate the importance of keeping the measurements very close to the target source surface.

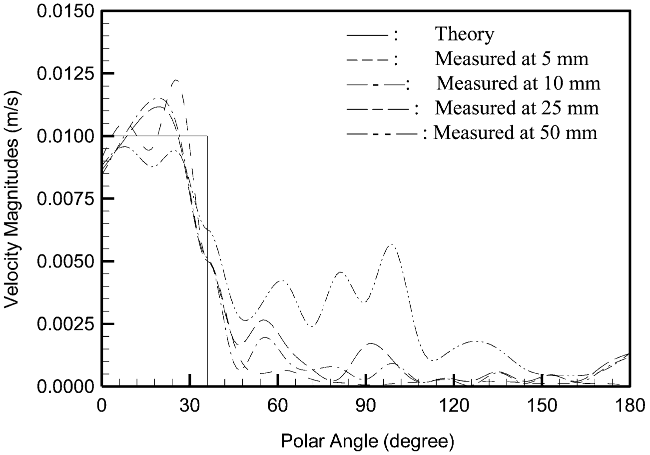

Fig. 6.5 Comparison of the reconstructed normal component of velocity on the surface of a partially vibrating sphere $ka = 1.46$ using the CHELS method based on measurements taken at different radial distances

Example 6.2 Consider a simplified engine block with an overall length of 0.460 m, overall width of 0.435 m, and overall height of 0.630 m. To test the effectiveness of the CHELS method, sharp edges and corners and abrupt changes in surface contours are built in this model. For such arbitrary geometry, analytic solutions do not exist and numerical solutions must be sought.

To simulate acoustic radiation from this engine block in a free field, harmonic excitations of different amplitudes are assumed on three arbitrarily selected surfaces: 5×10^5 N/m^2 on the top and 2×10^5 N/m^2 on part of the front and back surfaces at various frequencies (see Fig. 6.6). The bottom of the engine block is clamped with zero displacement and slope, and the rest surfaces are left unconstrained. The normal surface velocity distributions are obtained using the standard FEM codes and the surface acoustic pressures are specified using the BEM codes with 1,548 triangular elements and 776 discrete nodes. Once the surface acoustic quantities are specified, field acoustic pressures are calculated.

To reconstruct the surface acoustic quantities using the CHELS method, we take $M = 277$ measurement points over an imaginary sphere of radius $r = 0.408$ m that encloses the engine block, which is much fewer than 776 points. In particular, we select $M_1 = 56$ as input to set up the HELS formulations and $M_2 = 221$ to optimize the number of expansion functions. For the frequency range considered, this optimal value is found to be approximately $J_{\mathrm{op}} = 22$. Once this is done, the acoustic pressures on the measurement surface are regenerated by Eq. (6.56). The results are taken as input data to Eqs. (6.57) and (6.58) to reconstruct the surface acoustic quantities.

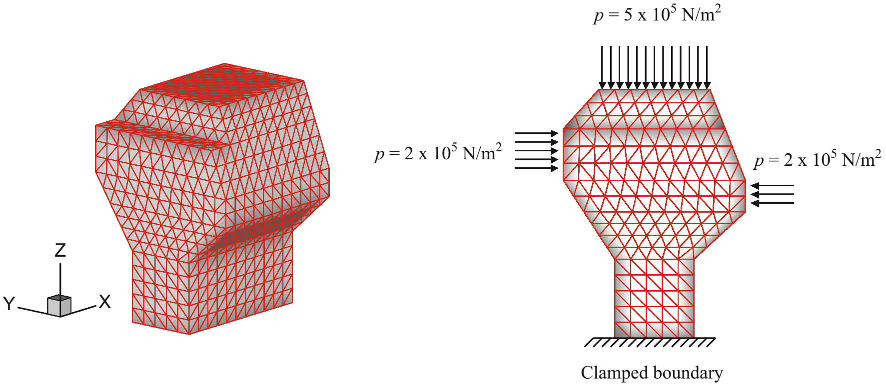

Fig. 6.6 Schematic of an engine block subject to distributed harmonic force excitations

Note that one can divide the measurements into two groups of any sizes. However, for an arbitrarily shaped surface, the clearance between the measurement and source surfaces may vary from one point to another. As a result, the amounts of the evanescent waves captured in the input data may be different. To minimize the impact of the loss of evanescent waves in reconstruction, a low-pass filter must be used to eliminate the evanescent waves that drop below the background noise level. This is equivalent to specifying the optimal expansion number J_{op}. Experiment results indicate that in most cases it is better to select a smaller value for M_1 and a larger value for M_2 to achieve the desired reconstruction.

It is emphasized that even if all steps as suggested above are followed, it will be unrealistic to expect ideal reconstruction. This is because: (1) measurements are taken on a spherical surface, not a conformal surface, and (2) the number of measurement points is greatly reduced in CHELS to alleviate the complexities involved taking an excessive number of measurements demanded by the BEM-based NAH.

Also noted is the fact that the accuracy of reconstruction varies with frequency. To ensure that measurements are taken in the near field, we gauge the standoff distance d with respect to the critical spatial wavelength λ_{cr}, which is set at $\lambda_{\text{cr}} = \pi a/8$, and require that the following conditions be satisfied: (1) $d \ll a$, and (2) $d \ll \lambda_{\text{cr}}$. Because in the CHELS method the standoff distance d is nonuniform, we take the maximum clearance between the measurement and source surfaces $d_{\max}$. Therefore, these conditions are rewritten as $d_{\max} \ll a$ and $d_{\max} \ll \lambda_{\text{cr}} = \pi a/8$.

In this case the characteristic dimension of the engine is $a = (0.435 + 0.460 + 0.630)/3 = 0.508$ m and the maximum clearance between measurement and source surface is $d_{\max} = 0.19$ m < 0.508 m, so the first condition is satisfied. However, the second condition is not because $d_{\max} = 0.19$ m and $\lambda_{\text{cr}} = \pi a/8 = 0.197$ m. As a result, some near-field information is lost in the input data.

In what follows, we present the reconstructed acoustic fields on the engine block surfaces based on $M = 277$ measurement points. For validation purposes, we use

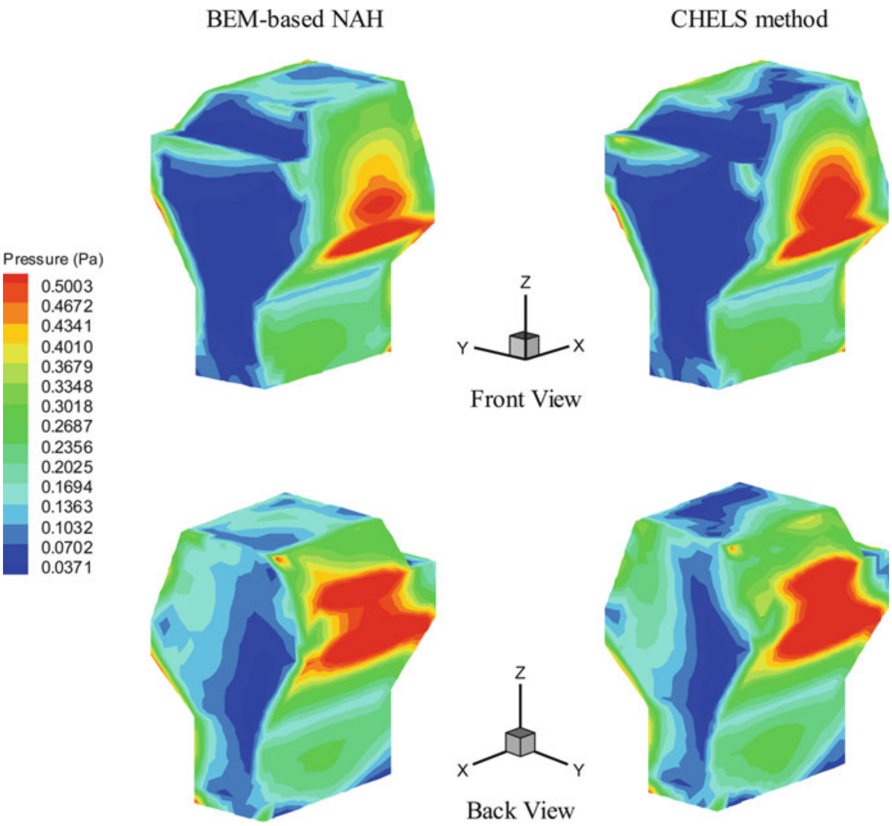

Fig. 6.7 Comparison of the reconstructed acoustic pressure distributions over the surfaces of engine block using the CHELS method with $M = 277$ data points (*right column*) and benchmark values with $M = 776$ data points (*left column*) at $ka = 1$

Eq. (6.3-6) to reconstruct the surface acoustic quantities based on $M = 776$ measurement points, which are the same as the discrete nodes. Figures 6.7 and 6.8 display the comparisons of the reconstructed acoustic pressure and normal velocity distributions on the surfaces of the engine block by using the CHELS method and benchmark values, respectively, at $ka = 1$.

It is emphasized that this engine block represents a fairly complex structure that contains sharp edges, corners, and abrupt changes along the surface contours. Yet satisfactory reconstruction is obtained by using the CHELS method with a reduction in input data points by more than 63 %. In contrast, when data points are reduced to one-half, $M = 386$, aliasing occurs in the reconstructed acoustic quantities obtained by using the BEM-based NAH because input data are severely under sampled (see Fig. 6.9) [100].

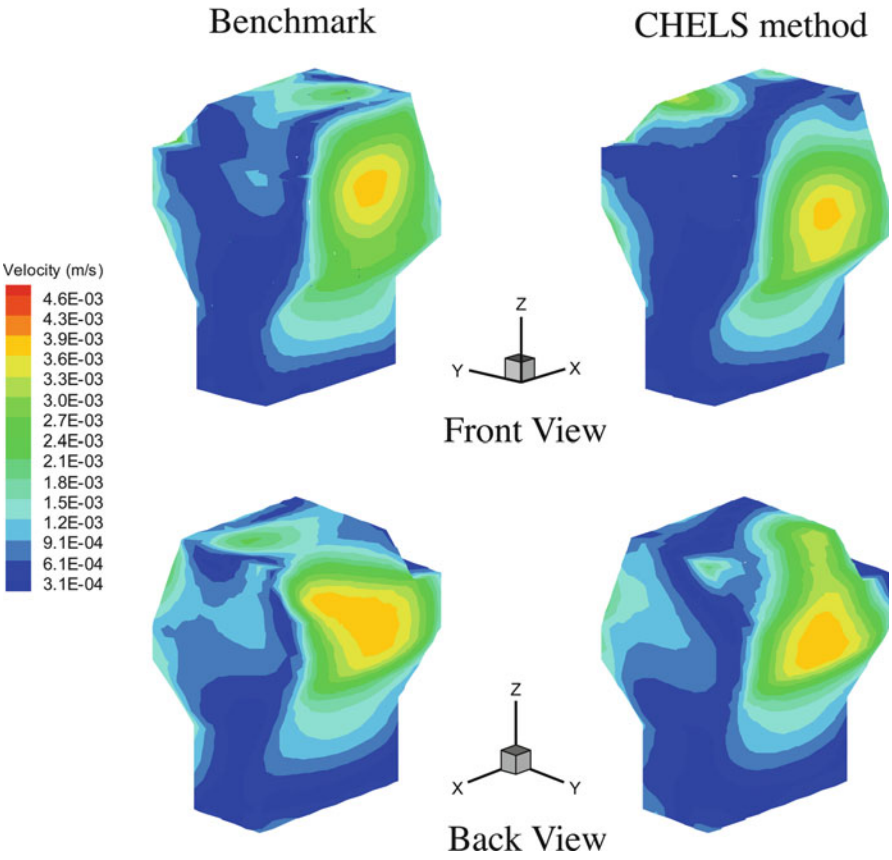

Fig. 6.8 Comparison of the reconstructed normal surface velocity distributions over the surfaces of engine block using the CHELS method with $M = 277$ data points (*right column*) and benchmark values with $M = 776$ data points (*left column*) at $ka = 1$

Equations (6.57) and (6.58) can be used to reconstruct acoustic radiation in the far field by setting the reconstruction point at $\vec{x}_s^{\,\text{rec}} = \vec{x}^{\,\text{rec}}$. This is straightforward because all field points are now outside the minimum sphere, so the acoustic field can be adequately represented by the outgoing spherical waves. Moreover, the loss of the evanescent waves has a negligible impact on reconstruction [101].

Figure 6.10 demonstrates comparisons of the reconstructed normal component of the time-averaged acoustic intensity by using the CHELS method on two planes ($2.6 \times 2.6\ \text{m}^2$) at $y = \pm 3$ m measured from the center of the engine block versus the BEM results. Note that the peak amplitude of the time-averaged intensity on the front plane is slightly lower than that of the back plane. This is because more forces are acting on the backside than on the front side of the engine block.

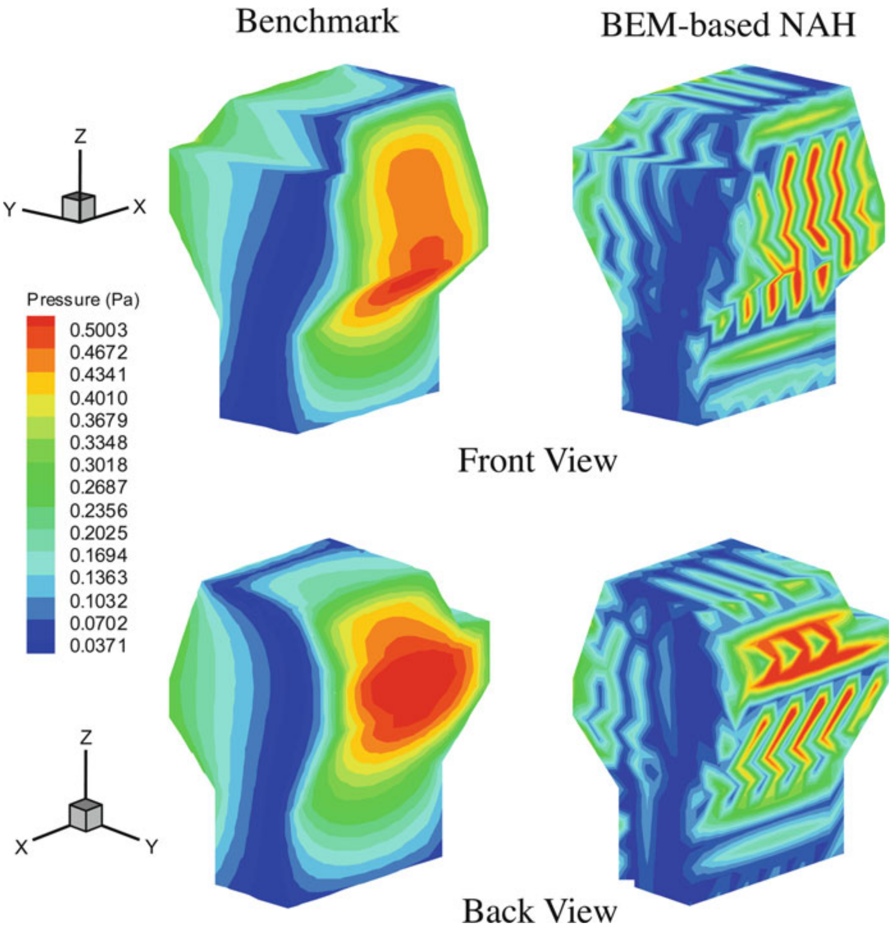

Fig. 6.9 Comparison of the reconstructed acoustic pressure distributions on the engine block surfaces by using the BEM-based NAH with $M = 388$ input data point and the benchmark results. In this case, aliasing occurs because the input data are severely under sampled

These results demonstrate that the CHELS method can be used to enhance the efficiency in reconstruction by taking relatively fewer measurement points on a minimum sphere enclosing the target source, yet still allowing for a relatively accurate reconstruction of the acoustic quantities. This is done by setting up the HELS formulations using a finite number measurement points, and regenerating as many acoustic pressures as those required by the BEM-based NAH to reconstruct the acoustic quantities on the source surface as well as in the field.

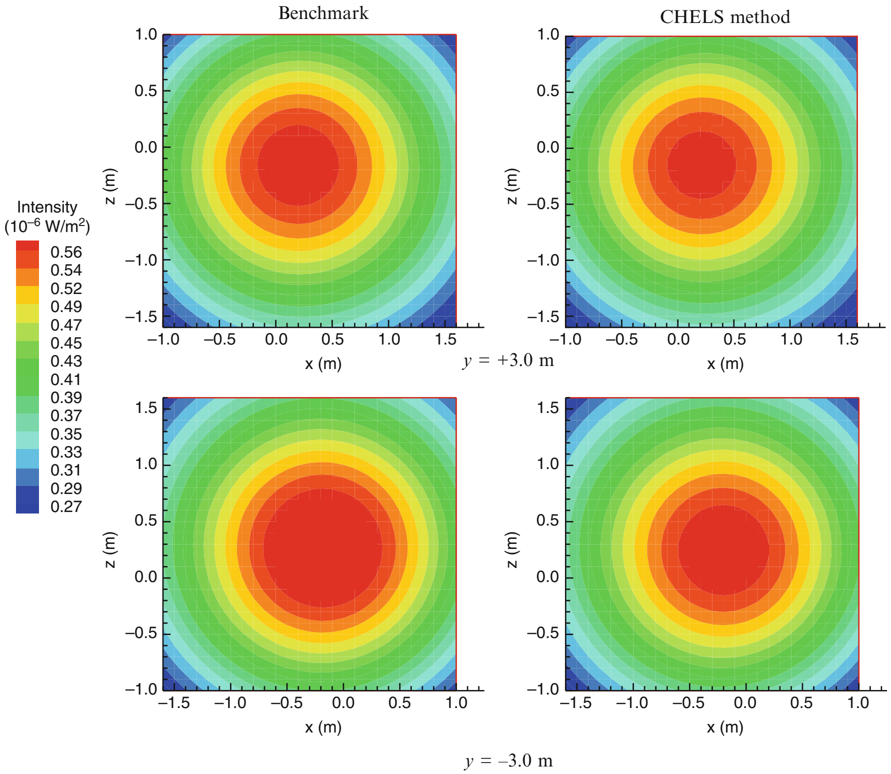

Fig. 6.10 Comparison of the reconstructed normal component of the time-averaged acoustic intensity distribution over two planes at $y = \pm 3.0$ m measured with respect to the center of the engine block using the CHELS method (*right column*) and BEM-based NAH (*left column*) at $ka = 1$

Problems

6.1. What are the differences between the Helmholtz equation and surface Helmholtz integral equation (6.25)?

6.2. Show that the surface Helmholtz integral equation can be derived by taking the limit as the field point $\vec{x}$ approaches the surface point $\vec{x}_s$ in Eq. (6.10).

6.3. Show that the surface Helmholtz integral equation (6.25) fails to yield a unique solution when the frequency approaches one of the Dirichlet eigenvalue for the interior region.

6.4. Consider the acoustic pressure inside an arbitrarily shaped enclosure as shown in Fig. 5.9. Follow the same procedures as shown in Sect. 6.1 and derive the Helmholtz integral formulation for the interior region. What is the surface over which the integration are taken in this case?

6.5. Continue Problem 6.4 and derive the surface Helmholtz integral equation for the interior region by taking the limit as $\vec{x} \to \vec{x}_s$ from the inside.

6.6. Continue Problem 6.5 and discuss whether the surface Helmholtz integral equation for the interior region suffers from the same nonuniqueness difficulty at certain eigenfrequencies as that for the exterior region.

6.7. Discuss how to determine the acoustic pressure radiated from a vibrating surface by using the Helmholtz integral theory. Outline the steps required in solving this problem.

6.8. What is the CHELS method? What are the advantages and limitations of the CHELS method compared with the HELS- and BEM-based NAH?

6.9. Discuss the implementation of the CHELS method and compare it to that of HELS method.

6.10. Discuss the implementation of the CHELS method and compare it to that of BEM-based NAH.